

The NaK $1^3\Delta$ states: Theoretical and experimental studies of fine and hyperfine structure of rovibrational levels near the dissociation limit

A. D. Wilkins, L. Morgus,^{a)} J. Hernandez-Guzman,^{b)} J. Huennekens,^{c)} and A. P. Hickman^{d)}
Department of Physics, Lehigh University, Bethlehem, Pennsylvania 18015

(Received 7 June 2005; accepted 8 July 2005; published online 27 September 2005)

Earlier high-resolution spectroscopic studies of the fine and hyperfine structure of rovibrational levels of the $1^3\Delta$ state of NaK have been extended to include high lying rovibrational levels with $v \leq 59$, of which the highest levels lie within $\sim 4 \text{ cm}^{-1}$ of the dissociation limit. A potential curve is determined using the inverted perturbation approximation method that reproduces these levels to an accuracy of $\sim 0.026 \text{ cm}^{-1}$. For the largest values of v , the outer turning points occur near $R \sim 12.7 \text{ \AA}$, which is sufficiently large to permit the estimation of the C_6 coefficient for this state. The fine and hyperfine structure of the $1^3\Delta$ rovibrational levels has been fit using the matrix diagonalization method that has been applied to other states of NaK, leading to values of the spin-orbit coupling constant A_v and the Fermi contact constant b_F . New values determined for $v \leq 33$ are consistent with values determined by a simpler method and reported earlier. The measured fine and hyperfine structure for v in the range $44 \leq v \leq 49$ exhibits anomalous behavior whose origin is believed to be the mixing between the $1^3\Delta$ and $1^1\Delta$ states. The matrix diagonalization method has been extended to treat this interaction, and the results provide an accurate representation of the complicated patterns that arise. The analysis leads to accurate values for A_v and b_F for all values of $v \leq 49$. For higher v ($50 \leq v \leq 59$), several rovibrational levels have been assigned, but the pattern of fine and hyperfine structure is difficult to interpret. Some of the observed features may arise from effects not included in the current model. © 2005 American Institute of Physics.
 [DOI: [10.1063/1.2010471](https://doi.org/10.1063/1.2010471)]

I. INTRODUCTION

A program of high-resolution spectroscopic studies in our laboratory has probed the fine and hyperfine structure of several excited triplet states of NaK.¹⁻⁴ Sodium-potassium mixtures are of current interest for mixed species atom traps, and the NaK high lying triplet states are of particular interest for the understanding of future sodium-potassium photoassociation spectra. Our previous investigation of the $1^3\Delta$ state¹ reported fine and hyperfine structure of numerous rovibrational levels for $v \leq 33$. This work provided a Rydberg-Klein-Rees (RKR) potential for the $1^3\Delta$ state as well as experimental values of the spin-orbit coupling constant A_v and the Fermi contact constant b_F for the vibrational levels probed. The present paper reports the investigation of significantly higher vibrational levels for the $1^3\Delta$ state and also the application of more elaborate theoretical tools to the analysis of the spectra. An enhanced theoretical analysis is needed at larger v and N because the effects of the fine and hyperfine structure terms in the molecular Hamiltonian can be of comparable size, and intermediate angular momentum coupling schemes must be invoked to interpret the observed spectra. In addition, several features are observed in the spectra that

appear to arise from coupling between the $1^1\Delta$ and $1^3\Delta$ states. The theoretical analysis of the spectra is generalized to include this interaction as well.

As in our previous work,¹⁻⁴ we use the technique of “perturbation-facilitated, optical-optical double resonance” (PFOODR) spectroscopy⁵⁻²⁸ to measure the spectra of excited triplet states. This technique involves two-step excitation from the singlet ground state to a highly excited triplet state through specific intermediate state rovibrational “window” levels that display both singlet and triplet character due to perturbations. When one uses narrow band continuous wave (cw) lasers (as we do), this technique is also capable of very high resolution since it is inherently Doppler-free. Additional studies using this method are cited in our previous work. The theoretical analysis we report here is based on the matrix diagonalization method that we have used before to analyze the fine and hyperfine structure of the NaK $4^3\Sigma^+$ state² and the $1(b)^3\Pi_{\Omega=0}$ component of the window levels.³

This paper is organized as follows: Section II briefly describes the experiment and the data obtained. Section III describes the theory. The main results are presented and discussed in Sec. IV, and Sec. V contains concluding remarks.

II. EXPERIMENT

The experimental setup is the same as that used in Ref. 1 and is shown in Fig. 1 of that reference. Briefly, a mixture of sodium and potassium is contained in a four-arm cross heat-pipe oven and heated to a temperature between 361 and

^{a)}Current address: Department of Physics, Drew University, 36 Madison Ave., Madison, NJ 07940.

^{b)}Current address: Department of Physics, Emory University, 400 Dowman Dr., Atlanta, GA 30322.

^{c)}Electronic address: jph7@lehigh.edu

^{d)}Electronic address: aph2@lehigh.edu

395 °C. This produces a vapor containing K₂, NaK, and Na₂ molecules, in addition to sodium and potassium atoms. Argon buffer gas at a pressure of ~0.5–2 Torr is used to keep the alkali vapor from reacting with the oven windows, which are cooled to room temperature using external cooling coils.

Rovibrational levels of the NaK 1³Δ state are accessed by PFOODR spectroscopy. The sequence of transitions is $1^3\Delta(v, N, J) \leftarrow 1(b)^3\Pi_{\Omega=0}(v_b, J') \sim 2(A)^1\Sigma^+(v_A, J') \leftarrow 1(X)^1\Sigma^+(v_X, J' \pm 1)$. The intermediate levels $1(b)^3\Pi_{\Omega=0}(v_b, J') \sim 2(A)^1\Sigma^+(v_A, J')$ have mixed singlet-triplet character due to spin-orbit perturbations between nearly degenerate levels of the two electronic states with the same rotational quantum number J' . Such levels are called “window” levels because they provide access from the singlet ground state to various triplet states, and a number of these levels for NaK have been listed in previous work.^{3,4} A tunable, single-mode, cw dye laser (Coherent 699-29) is used as the “pump” laser to excite NaK molecules on specific $1(b)^3\Pi_{\Omega=0}(v_b, J') \sim 2(A)^1\Sigma^+(v_A, J') \leftarrow 1(X)^1\Sigma^+(v_X, J' \pm 1)$ transitions. The transition of interest is found by observing $2(A)^1\Sigma^+(v_A, J') \rightarrow 1(X)^1\Sigma^+$ fluorescence emitted at right angles to the laser propagation axis with a free-standing photomultiplier tube (PMT) equipped with a 700–1000 nm bandpass filter while the pump laser frequency is scanned. Once the transition is found, the pump laser frequency is fixed to line center of the transition. A tunable, single-mode, cw Ti:sapphire laser (Coherent 899-29) is used as the “probe” laser to excite specific $1^3\Delta(v, N, J) \leftarrow 1(b)^3\Pi_{\Omega=0}(v_b, J') \sim 2(A)^1\Sigma^+(v_A, J')$ transitions, which are found by observing green $3^3\Pi \rightarrow 1(a)^3\Sigma^+$ fluorescence using a second free-standing PMT equipped with appropriate filters. In this case, the upper $3^3\Pi$ state is collisionally populated from the laser excited level, $1^3\Delta(v, N, J)$. The two laser beams counterpropagate through the oven, and the total green fluorescence signal is recorded as the probe laser frequency is scanned. As discussed in Ref. 1, the hyperfine structure of the intermediate state is canceled for the most part in the counterpropagating beam geometry. Thus the excitation spectra map out the fine and hyperfine structure of the upper level $1^3\Delta(v, N)$. These spectra present a distinctive signature pattern, which is discussed in Sec. IV A and which was shown earlier in Figs. 2 and 4 of Ref. 1. This pattern makes the $1^3\Delta$ spectra easy to distinguish from excitations to other triplet states ($4^3\Sigma^+$ and $3^3\Pi$) that lie in the same energy range.^{2,4}

The pump laser wavemeter is calibrated by sending a small fraction of the beam through an iodine cell and comparing I₂ laser-induced fluorescence with lines listed in the iodine atlas.²⁹ The probe laser wavemeter is calibrated using optogalvanic signals from neon transitions in a hollow cathode lamp. We consider absolute energies of $1^3\Delta(v, N, J)$ levels recorded using the PFOODR technique in our setup to be accurate to within 0.02 cm⁻¹. However, splittings between hyperfine levels can be determined with much higher accuracy, typically 0.001 cm⁻¹ (30 MHz).

III. THEORY

A. Fine and hyperfine structure of ³Δ states

Our analysis of the fine and hyperfine structure of the $1^3\Delta$ state is based on the same methodology that we applied in previous work on the $4^3\Sigma^+$ state of NaK.² We summarize this method briefly, and then we will describe the generalization to include the interaction with the $1^1\Delta$ state. Our starting point is the Hamiltonian^{30–35}

$$\hat{H} = \hat{H}_{\text{rot}} + A_v \mathbf{L} \cdot \mathbf{S} + b_F \mathbf{I} \cdot \mathbf{S} + \gamma \mathbf{N} \cdot \mathbf{S} + \epsilon(3\hat{S}_z^2 - \mathbf{S}^2), \quad (1)$$

where \hat{H}_{rot} is the rotational Hamiltonian, $A_v \mathbf{L} \cdot \mathbf{S}$ is the spin-orbit interaction, $b_F \mathbf{I} \cdot \mathbf{S}$ is the Fermi contact interaction,³⁶ which is the dominant contribution to the hyperfine structure of Rydberg states in alkali molecules,^{36–39} $\gamma \mathbf{N} \cdot \mathbf{S}$ is the spin-rotation term, and $\epsilon(3\hat{S}_z^2 - \mathbf{S}^2)$ is the spin-spin term. As usual, \mathbf{N} is the sum of the rotational angular momentum of the nuclei (\mathbf{R}) plus the electron orbital angular momentum (\mathbf{L}); \mathbf{S} is the total electron spin, and \mathbf{I} is the nuclear spin. We take \mathbf{I} to be the nuclear spin of Na only, since the nuclear magnetic moment of Na is much larger than that of K, and since the electron density at the Na nucleus is also larger for this electronic state.^{3,40}

We formulate the coupling using Hund’s case ($b_{\beta I}$) coupling scheme,

$$\mathbf{N} + \mathbf{S} = \mathbf{J}, \quad \mathbf{J} + \mathbf{I} = \mathbf{F}. \quad (2)$$

We find the eigenvalues of \hat{H} by direct diagonalization of the matrix representation of Eq. (1), using basis functions $|\alpha NSJI; FM_F\rangle$ that are eigenfunctions of N^2 , S^2 , J^2 , I^2 , F^2 , and M_F . These basis functions are constructed as linear combinations

$$|\alpha NSJI; FM_F\rangle = \sum_{M_J} \sum_{M_I} C(JM_J, IM_I; FM_F) |\alpha NSJM_J\rangle |IM_I\rangle, \quad (3)$$

where $C(\dots)$ is a Clebsch-Gordan coefficient, and the kets on the rhs are direct products of Hund’s case (b) basis functions (with no nuclear spin) and nuclear spin functions. This expression allows us to evaluate all matrix elements of the general basis functions $|\alpha NSJI; FM_F\rangle$ using, for example, the expressions derived by Kovács³⁰ for Hund’s case (b). Our previous work² contains explicit expressions for the matrix elements of several terms in Eq. (1). Here we concentrate on the spin-orbit term, which was zero for the case we considered in Ref. 2. We will generalize our analysis to include singlet and triplet mixing, and we will present explicit expressions in the next section.

B. Treatment of ¹Δ–³Δ mixing

In this section we will summarize the analysis of the coupling between $1^1\Delta$ and $3^3\Delta$ levels. We consider a system consisting of a Na atom in the $3s$ level and a K atom in the $3d$ level. We will attribute the fine structure splitting to the atomic K spin-orbit operator $\hat{H}_{\text{so}}^{(K)}$, although later we will make the connection to the molecular NaK system. Let \mathbf{s}_1 and \mathbf{s}_2 be the spins of Na($3s$) and K($3d$), respectively, and let

\mathbf{I}_1 and \mathbf{I}_2 be the corresponding orbital angular momenta. Both electron spins are $\frac{1}{2}$, that is, $s_1=s_2=\frac{1}{2}$. Also, $l_1=0$ and $l_2=2$. Then the spin-orbit operator for atomic K may be written

$$\hat{\mathbf{H}}_{\text{so}}^{(\text{K})} = A\mathbf{I}_2 \cdot \mathbf{s}_2. \quad (4)$$

We consider the matrix elements of this operator in different coupling schemes in the molecular frame.

The first scheme is jj coupling, in which the angular momentum of each atom is defined first. This scheme may be written

$$\mathbf{j}_1 = \mathbf{I}_1 + \mathbf{s}_1 = \mathbf{s}_1, \quad \mathbf{j}_2 = \mathbf{I}_2 + \mathbf{s}_2, \quad \mathbf{J}_a = \mathbf{j}_1 + \mathbf{j}_2. \quad (5)$$

The total electronic and spin angular momentum is \mathbf{J}_a , and its projection on the internuclear axis is Ω . Since $\mathbf{I}_1=0$, $j_1=s_1=\frac{1}{2}$, and we can write the general basis functions in this scheme as

$$|s_1s_2l_2(j_2); J_a\Omega\rangle. \quad (6)$$

The value of j_2 for the K atom in the $3d$ state can be either $\frac{3}{2}$ or $\frac{5}{2}$. The matrix elements of $\hat{\mathbf{H}}_{\text{so}}^{(\text{K})}$ are diagonal in the jj basis functions:

$$\begin{aligned} \langle s_1s_2l_2(j_2); J_a\Omega | \hat{\mathbf{H}}_{\text{so}}^{(\text{K})} | s_1s_2l_2(j_2'); J_a'\Omega' \rangle \\ = \delta_{j_2j_2'} \delta_{J_aJ_a'} \delta_{\Omega\Omega'} E_{j_2}, \end{aligned} \quad (7)$$

where $E_{3/2}$ and $E_{5/2}$ are the energies of the two K($3d$) fine structure levels. The splitting between these states is 2.33 cm^{-1} ; the ordering is inverted ($E_{5/2} < E_{3/2}$) because the sign of the fine structure constant is negative.

The next coupling scheme we consider is LS coupling, which corresponds to

$$\mathbf{S} = \mathbf{s}_1 + \mathbf{s}_2, \quad \mathbf{L} = \mathbf{I}_1 + \mathbf{I}_2 = \mathbf{I}_2, \quad \mathbf{J}_a = \mathbf{L} + \mathbf{S}. \quad (8)$$

The basis states are written

$$|s_1s_2(S)l_2; J_a\Omega\rangle. \quad (9)$$

A variation of LS coupling that we call LS' coupling is the most useful for making the connection with the formalism of Sec. III A. The basis functions of this set are

$$|s_1s_2(S\Sigma)l_2\Lambda\rangle. \quad (10)$$

These basis functions correspond to a scheme that is the same as the LS scheme defined by Eq. (8), except that \mathbf{L} and \mathbf{S} do not couple to form \mathbf{J}_a . We want the projections Λ and Σ of the total L and S on the internuclear axis (z) to be good quantum numbers, so that we can identify this basis with Hund's case (a). (We take Λ and Σ to be signed.)

The transformation between the jj basis and the LS' basis may be derived using standard techniques.⁴¹ The result is

$$\langle s_1s_2(S\Sigma)l_2\Lambda | s_1s_2l_2(j_2); J_a\Omega \rangle = \delta_{\Omega, \Sigma+\Lambda} (-1)^{s_1+s_2+S+J_a-\Omega} \sqrt{(2S+1)(2J_a+1)(2j_2+1)} \begin{pmatrix} S & l_2 & J_a \\ \Sigma & \Lambda & -\Omega \end{pmatrix} \begin{Bmatrix} s_1 & s_2 & S \\ l_2 & J_a & j_2 \end{Bmatrix}. \quad (11)$$

We have used Eq. (11) to transform the matrix elements of $\hat{\mathbf{H}}_{\text{so}}^{(\text{K})}$ to the LS' basis. Since $\Omega=\Sigma+\Lambda$ is conserved, $\hat{\mathbf{H}}_{\text{so}}^{(\text{K})}$ is block diagonal in Ω . The only blocks in which both $^1\Delta$ and $^3\Delta$ states appear are those for $\Omega=\pm 2$. We only need to consider $\Omega=2$, since the analysis is identical for $\Omega=-2$. The $\Omega=2$ block of the matrix representation of $\hat{\mathbf{H}}_{\text{so}}^{(\text{K})}$ is given by

$$\begin{array}{c|ccc} & ^1\Delta_{\Omega=2} & ^3\Pi_{\Omega=2} & ^3\Delta_{\Omega=2} \\ \hline ^1\Delta_{\Omega=2} & \frac{2}{5}E_{3/2} + \frac{3}{5}E_{5/2} & \sqrt{\frac{2}{25}}(E_{3/2} - E_{5/2}) & -\frac{2}{5}(E_{3/2} - E_{5/2}) \\ ^3\Pi_{\Omega=2} & \sqrt{\frac{2}{25}}(E_{3/2} - E_{5/2}) & \frac{1}{5}E_{3/2} + \frac{4}{5}E_{5/2} & -\sqrt{\frac{2}{25}}(E_{3/2} - E_{5/2}) \\ ^3\Delta_{\Omega=2} & -\frac{2}{5}(E_{3/2} - E_{5/2}) & -\sqrt{\frac{2}{25}}(E_{3/2} - E_{5/2}) & \frac{2}{5}E_{3/2} + \frac{3}{5}E_{5/2} \end{array}. \quad (12)$$

We now make the assumption that the coupling with the $^3\Pi$ state is weak (it will generally be far removed in energy from the $^1\Delta$ and $^3\Delta$ states). Dropping the terms involving the $^3\Pi$ state [the second row and column in Eq. (12)] we find that $\hat{\mathbf{H}}_{\text{so}}^{(\text{K})}$ for $\Omega=2$ takes the form

$$\begin{array}{c|cc} & ^1\Delta_{\Omega=2} & ^3\Delta_{\Omega=2} \\ \hline ^1\Delta_{\Omega=2} & \frac{2}{5}E_{3/2} + \frac{3}{5}E_{5/2} & -\frac{2}{5}(E_{3/2} - E_{5/2}) \\ ^3\Delta_{\Omega=2} & -\frac{2}{5}(E_{3/2} - E_{5/2}) & \frac{2}{5}E_{3/2} + \frac{3}{5}E_{5/2} \end{array}.$$

The only Δ state that can have $\Omega=1$ or $\Omega=3$ is the $^3\Delta$. Adding these states to the subset of the LS' basis functions we're using, we obtain the following matrix representation:

	${}^3\Delta_{\Omega=1}$	${}^3\Delta_{\Omega=2}$	${}^1\Delta_{\Omega=2}$	${}^3\Delta_{\Omega=3}$
${}^3\Delta_{\Omega=1}$	$\frac{4}{5}E_{3/2} + \frac{1}{5}E_{5/2}$	0	0	0
${}^3\Delta_{\Omega=2}$	0	$\frac{2}{5}E_{3/2} + \frac{3}{5}E_{5/2}$	$-\frac{2}{5}(E_{3/2} - E_{5/2})$	0
${}^1\Delta_{\Omega=2}$	0	$-\frac{2}{5}(E_{3/2} - E_{5/2})$	$\frac{2}{5}E_{3/2} + \frac{3}{5}E_{5/2}$	0
${}^3\Delta_{\Omega=3}$	0	0	0	$E_{5/2}$

(13)

Written in this form, $\hat{\mathbf{H}}_{\text{so}}^{(\text{K})}$ clearly retains its block diagonal structure with respect to Ω . To make the connection with the pure triplet case, it is convenient to reorder the basis functions so that the three ${}^3\Delta$ states are first. We also define

$$A = \frac{2}{5}(E_{5/2} - E_{3/2}), \quad (14)$$

and we define the zero of energy to be the degeneracy-weighted average \bar{E} of the $\text{K}(3d)$ fine structure energies:

$$\bar{E} = \frac{2}{5}E_{3/2} + \frac{3}{5}E_{5/2}. \quad (15)$$

With these manipulations, we obtain the following simple form for $\hat{\mathbf{H}}_{\text{so}}^{(\text{K})}$ in the basis of four LS' electronic functions, assuming a fixed molecular axis:

	${}^3\Delta_{\Omega=1}$	${}^3\Delta_{\Omega=2}$	${}^3\Delta_{\Omega=3}$	${}^1\Delta_{\Omega=2}$
${}^3\Delta_{\Omega=1}$	$-A$	0	0	0
${}^3\Delta_{\Omega=2}$	0	0	0	A
${}^3\Delta_{\Omega=3}$	0	0	A	0
${}^1\Delta_{\Omega=2}$	0	A	0	0

(16)

The eigenvalues of the above matrix are $-A$, $-A$, A , and A , corresponding to a splitting of $2A$ for the fine structure lev-

els. This result is not quite right, since from Eq. (14), the splitting should be $\frac{5}{2}A$. The discrepancy arises because we neglected the ${}^3\Pi$ states with $\Omega=2$. However, if we identify A with ΛA_v , the upper 3×3 block of Eq. (16) corresponds exactly to the spin-orbit interaction of a triplet state in the molecular limit (for Hund's case (a)). We will take Eq. (16) to be our model of the fine structure interaction for molecular NaK, treating A_v as an empirical coupling constant that must be adjusted to fit the data for each vibrational level.

The matrix given in Eq. (16) is the essential term for coupling the levels of the $1^3\Delta$ and $1^1\Delta$ electronic states. However, the complete calculation must also include vibrational, rotational, and hyperfine coupling terms; our existing code includes these terms using a Hund's case (b) basis because of the simplicity of the hyperfine coupling term in that basis. If we set $A = \Lambda A_v$ and transform Eq. (16) to case (b), we obtain

$$A_v \begin{pmatrix} \frac{\Lambda^2}{J} & \frac{\Lambda}{\sqrt{2}} \sqrt{\frac{(J^2 - \Lambda^2)(J+1)}{J^2(J+\frac{1}{2})}} & 0 & -\frac{\Lambda}{\sqrt{2}} \sqrt{\frac{(J+\Lambda)(J+1+\Lambda)}{J(J+1)}} \langle v'|v \rangle \\ \frac{\Lambda}{\sqrt{2}} \sqrt{\frac{(J^2 - \Lambda^2)(J+1)}{J^2(J+\frac{1}{2})}} & -\frac{\Lambda^2}{J(J+1)} & \frac{\Lambda}{\sqrt{2}} \sqrt{\frac{J[(J+1)^2 - \Lambda^2]}{(J+\frac{1}{2})(J+1)^2}} & \frac{\Lambda^2}{\sqrt{J(J+1)}} \langle v'|v \rangle \\ 0 & \frac{\Lambda}{\sqrt{2}} \sqrt{\frac{J[(J+1)^2 - \Lambda^2]}{(J+\frac{1}{2})(J+1)^2}} & -\frac{\Lambda^2}{J+1} & \frac{\Lambda}{\sqrt{2}} \sqrt{\frac{(J+1+\Lambda)(J+1-\Lambda)}{(J+\frac{1}{2})(J-1)}} \langle v'|v \rangle \\ -\frac{\Lambda}{\sqrt{2}} \sqrt{\frac{(J+\Lambda)(J+1+\Lambda)}{J(J+1)}} \langle v'|v \rangle & \frac{\Lambda^2}{\sqrt{J(J+1)}} \langle v'|v \rangle & \frac{\Lambda}{\sqrt{2}} \sqrt{\frac{(J+1+\Lambda)(J+1-\Lambda)}{(J+\frac{1}{2})(J-1)}} \langle v'|v \rangle & 0 \end{pmatrix}, \quad (17)$$

where $\Lambda=2$, and the basis functions are $|aNSJ\Omega\rangle$ in the order $N=J-1, J, J+1$ for triplet states ($S=1$) and $N=J$ for the singlet state ($S=0$). The upper 3×3 block of the matrix in Eq. (17) is exactly the same as the result of Kovács³⁰ for the spin-orbit operator. Note that the singlet-triplet coupling terms in the last row and column contain the overlap matrix

elements $\langle v'|v \rangle$ between the appropriate vibrational wave functions of the $1^1\Delta$ and $1^3\Delta$ rovibrational levels. The approximations leading to this result are discussed later in Sec. IV B. The matrix that represents the vibrational and rotational terms may be written [for a fixed J , in Hund's case (b)] as

$$\begin{pmatrix} E_{\text{trip}}^0(v, N=J-1, J) & 0 & 0 & 0 \\ 0 & E_{\text{trip}}^0(v, N=J, J) & 0 & 0 \\ 0 & 0 & E_{\text{trip}}^0(v, N=J+1, J) & 0 \\ 0 & 0 & 0 & E_{\text{sing}}^0(v', J) \end{pmatrix}. \quad (18)$$

The total Hamiltonian is represented by the sum of the matrices given in Eqs. (17) and (18), plus the hyperfine term $b_F \mathbf{I} \cdot \mathbf{S}$. We can evaluate the matrix elements of this sum in the 16 Hund's case ($b_{\beta J}$) functions $|\alpha NSJJ; FM_F\rangle$ listed in Table I using Eq. (3). This procedure is a straightforward generalization of the work we have done previously using only triplet states;²⁻⁴ in those cases we used only the upper 3×3 blocks of the matrices given by Eqs. (17) and (18).

IV. RESULTS AND DISCUSSION

A. Vibrational levels $0 \leq v \leq 33$: Experiment and Theory

In our previous work,¹ a total of 757 measurements of PFOODR transition frequencies representing 562 $1^3\Delta(v, N, J, e/f)$ rovibrational levels with $3 \leq v \leq 36$ were recorded using four $1(b)^3\Pi_{\Omega=0}(v_b, J') \sim 2(A)^1\Sigma^+(v_A, J')$ window levels with $J' = 15, 26, 38,$ and 45 . The most interesting feature of the data was the systematic variation of the pattern of the line splittings due to fine and hyperfine structure. Representative data are shown in Fig. 1. For low values of N , the three fine structure levels (labeled by $J=N-1, J=N,$ and $J=N+1$) are well split, and each is divided into a set of four closely spaced hyperfine levels. As N increases, however, the three fine structure levels move closer together and can no longer be separately identified. This behavior suggests variations in the relative importance of the spin-orbit coupling term ($A_v \mathbf{L} \cdot \mathbf{S}$) and the hyperfine coupling term ($b_F \mathbf{I} \cdot \mathbf{S}$).

Huennekens *et al.*¹ analyzed these data to determine values of A_v for each vibrational level. The hyperfine splittings were not explicitly included in the analysis; rather the average energy of each hyperfine multiplet was used to represent the corresponding fine structure level. Then a Hamiltonian matrix that included electronic, vibrational, rotational, and

TABLE I. List of states for $1^1\Delta$ and $1^3\Delta$ in Hund's case ($b_{\beta J}$).

No.	N	J	State	No.	N	J	State
1	$F-\frac{5}{2}$	$F-\frac{3}{2}$	$1^3\Delta$	9	$F+\frac{1}{2}$	$F-\frac{1}{2}$	$1^3\Delta$
2	$F-\frac{3}{2}$	$F-\frac{3}{2}$	$1^3\Delta$	10	$F+\frac{1}{2}$	$F+\frac{1}{2}$	$1^3\Delta$
3	$F-\frac{3}{2}$	$F-\frac{1}{2}$	$1^3\Delta$	11	$F+\frac{1}{2}$	$F+\frac{3}{2}$	$1^3\Delta$
4	$F-\frac{3}{2}$	$F-\frac{3}{2}$	$1^1\Delta$	12	$F+\frac{1}{2}$	$F+\frac{1}{2}$	$1^1\Delta$
5	$F-\frac{1}{2}$	$F-\frac{3}{2}$	$1^3\Delta$	13	$F+\frac{3}{2}$	$F+\frac{1}{2}$	$1^3\Delta$
6	$F-\frac{1}{2}$	$F-\frac{1}{2}$	$1^3\Delta$	14	$F+\frac{3}{2}$	$F+\frac{3}{2}$	$1^3\Delta$
7	$F-\frac{1}{2}$	$F+\frac{1}{2}$	$1^3\Delta$	15	$F+\frac{5}{2}$	$F+\frac{3}{2}$	$1^3\Delta$
8	$F-\frac{1}{2}$	$F-\frac{1}{2}$	$1^1\Delta$	16	$F+\frac{3}{2}$	$F+\frac{3}{2}$	$1^1\Delta$

spin-orbit interactions for each v was set up and diagonalized using the program LSQ.⁴² The spin-orbit parameter A_v was adjusted to obtain a least squares fit to the observed energies of the (v, N, J) levels. Subsequently, the best value for the Fermi contact constant b_F (the same value for all v 's) was determined by a perturbative treatment of the low N data ($N=15$). This two step approach was expected to be very reliable for levels such as those shown in Fig. 1 for low values of N , where the hyperfine splitting is considerably less than the fine structure splitting. However, for larger values of N , a more elaborate analysis is desirable.

We have completed such an analysis using the general matrix diagonalization method described in Sec. III A. We evaluated the eigenvalues of Eq. (1) for a large number of possible values of the parameters $b_F, A_v,$ and B_v . (We set $\gamma = \epsilon = 0$, because we found that those variables had a very small effect.) The results for a wide variety of calculations could be very well represented by a set of curves that relate "reduced energy levels" to a "reduced hyperfine coupling constant." These curves are shown in Fig. 2. The abscissa is $2b_F/S_0$, where S_0 is the average splitting of the fine structure

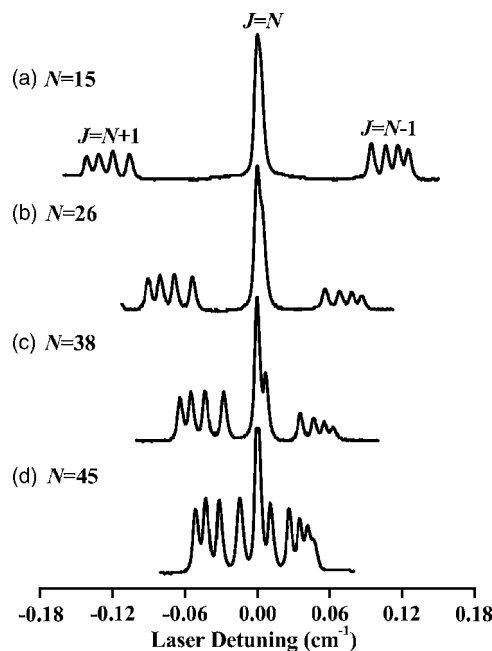


FIG. 1. Variation of the fine and hyperfine structure for a series of rovibrational levels of the $1^3\Delta$ state. (a) $1^3\Delta(v=10, N=15) \leftarrow 1(b)^3\Pi_{\Omega=0}(v_b=15, J'=15)$ transition, (b) $1^3\Delta(v=17, N=26) \leftarrow 1(b)^3\Pi_{\Omega=0}(v_b=17, J'=26)$ transition, (c) $1^3\Delta(v=10, N=38) \leftarrow 1(b)^3\Pi_{\Omega=0}(v_b=12, J'=38)$ transition, and (d) $1^3\Delta(v=14, N=45) \leftarrow 1(b)^3\Pi_{\Omega=0}(v_b=18, J'=45)$ transition. For smaller values of N , the fine structure components $J=N+1, J=N,$ and $J=N-1$ are well separated. As N increases, these components tend to merge. The dependence of the splitting on v is not significant for $10 \leq v \leq 17$.

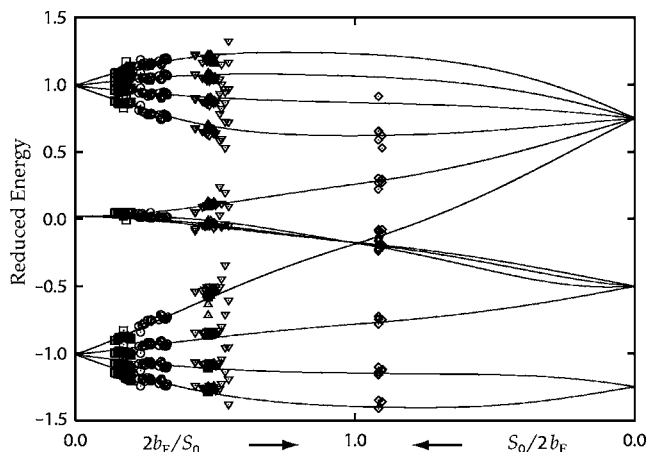


FIG. 2. Comparison of theory and experiment for the hyperfine splitting of the NaK $1^3\Delta$ state. The solid curves (—) show the relative spacing of the 12 hyperfine levels. The experimental data have been plotted in the same way. Data are shown for several different values of N : $N=15$ (\square), $N=26$ (\circ), $N=38$ (\triangle), $N=45$ (∇), $N=86$ and 87 (\diamond).

levels when the hyperfine interactions are ignored ($b_F=0$). The ordinate is determined by dividing all the energies by $\sqrt{(2b_F)^2 + (S_0^2)}$ and then shifting them so that the average value is zero. Such a scaling is suggested by the analysis of Condon and Shortley,⁴³ who used similar methods to describe the transition between LS and jj coupling. Figure 2 shows the relative spacings of the 12 hyperfine levels for the whole range of coupling strengths. On the left-hand side of the diagram $2b_F/S_0 \rightarrow 0$, corresponding to Hund's case ($b_{\beta j}$). In this case the hyperfine coupling is weak and we have, according to Eq. (2), three sets of four states since $I=3/2$. On the right-hand side, $2b_F/S_0 \rightarrow \infty$ ($S_0/2b_F \rightarrow 0$), corresponding to Hund's case ($b_{\beta S}$). For this case, the appropriate scheme is

$$\mathbf{G} = \mathbf{S} + \mathbf{I}, \quad \mathbf{F} = \mathbf{N} + \mathbf{G}, \quad (19)$$

leading to sets of two, four, and six states for $G=1/2, 3/2$, and $5/2$, respectively.

The general curves in Fig. 2 account well for the trends in the experimental data shown in Fig. 1. Smaller values of $2b_F/S_0$ correspond to lower values of N , so that the scans (a)–(d) in Fig. 1 correspond to moving rightward from $2b_F/S_0=0$ in Fig. 2. One can clearly see that as N increases, the splitting of the three groups of states for $J=N+1$, N , and $N-1$ gradually diminishes. Careful examination of scans (c) and (d) in Fig. 1 also reveals one of the four central states splitting off slightly to the right; the theoretical curves in Fig. 2 exactly reproduce this behavior.

Experimental data points have also been explicitly included in Fig. 2. These points were determined from several experimental scans for various values of v and J . We fit many scans together, using the experimentally determined values of B_v , a quadratic polynomial for the dependence of A_v on v , and a constant b_F (independent of v) to achieve the best fit. Once A_v and b_F were determined, we used them to determine appropriate values of S_0 and $2b_F/S_0$ so that the measured absolute energies could be converted to reduced energies and plotted on the diagram at the appropriate value of $2b_F/S_0$. The groups of points corresponding to the same N and different v are spread out by the dependence of A_v and

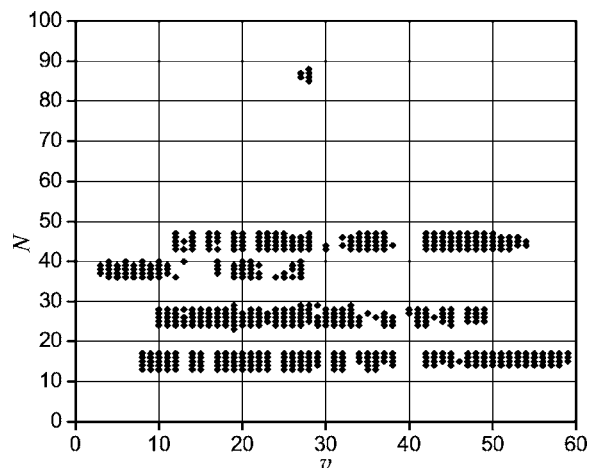


FIG. 3. The experimental data set.

B_v on v . Data corresponding to $N=15, 26, 38, 45, 86$, and 87 are shown. The agreement for a large number of data points is remarkably good. The data for $N=86$ and 87 ($2b_F/S_0 \approx 1$ at the center of the plot) were fit separately, but for all the other points we used four adjustable parameters and fit 1128 hyperfine energy levels. Many of the larger discrepancies may be attributed to localized perturbations.

The present calculations lead to slightly different best-fit values of A_v and b_F for the data reported by Huennekens *et al.*¹ However, the changes are very small, and in general the present results confirm the approximations of Ref. 1. The details will be presented in Sec. IV C.

B. New experimental data for $34 \leq v \leq 59$ and analysis of $^3\Delta-^1\Delta$ mixing

The present work reports many additional energy levels for the NaK $1^3\Delta$ state. The data set has been expanded to 1645 measurements of PFOODR transition frequencies representing 1083 $1^3\Delta(v, N, J, e/f)$ rovibrational levels with $3 \leq v \leq 59$. Most of the new data appear in the region $v \geq 34$. The same set of window levels allowed access to $1^3\Delta(v, N, J, e/f)$ levels with $N=J'-2, J'-1, J', J'+1, J'+2$ and $J=J'-1, J', J'+1$ where J' is the rotational quantum number of the window level (see Fig. 3 of Ref. 1), although a few levels with $v=27, 28, J=86, 87$, and 88 obtained using the window level $1(b)^3\Pi_{\Omega=0}(v_b=22, J'=87) \sim 2(A)^1\Sigma^+(v_A=28, J'=87)$ were added to the data set. All measured NaK $1^3\Delta(v, N, J, e/f)$ level energies are listed in EPAPS Table I of the supplementary Electronic Physics Auxiliary Publication Service (EPAPS) deposit.⁴⁴ Also listed in EPAPS Table I are the ground state, intermediate state, and upper $1^3\Delta$ state levels, as well as the pump and probe laser frequencies for each PFOODR transition studied in this work. Ground state energies are taken from Ref. 45. A pictorial view of the current data set is shown in Fig. 3.

The measured fine and hyperfine structure for v in the range $44 \leq v \leq 49$ exhibits anomalous behavior. An example is shown by the experimental scans in Fig. 4(b). These scans exhibit features that are qualitatively different from the behavior exhibited by the scans in Fig. 1. The left and right groups of states move asymmetrically with respect to the

central peak, and the left group even switches position with the middle group for $v=49$. In addition, the splitting of the central peak increases dramatically as v changes from 46 to 48. We were not able to fit these features using the model Hamiltonian of Eq. (1), but we were able to model them by invoking the mixing between the $^3\Delta$ and $^1\Delta$ states, as described in Sec. III B.

Including the singlet–triplet coupling introduces additional parameters into our model Hamiltonian. For each J we need the offset ΔE between the rovibrational levels for the $1^1\Delta$ and $1^3\Delta$ states before the effect of fine structure and hyperfine structure is added [cf. Eq. (18)]:

$$\Delta E = E_{\text{sing}}^0(v', J) - E_{\text{trip}}^0(v, N=J, J). \quad (20)$$

We also need the overlap matrix element $\langle v'|v\rangle$ between the vibrational wave functions [cf. Eq. (17)]. Unfortunately, the singlet level is not observed and the vibrational overlap is not known. However, even though the rovibrational spectrum of the $1^1\Delta$ state is not known, the shapes and equilibrium separations of the $1^1\Delta$ and $1^3\Delta$ states are very similar,^{46,47} and we can use the measured triplet state B_v values to estimate $E_{\text{sing}}^0(v', J\pm 1)$ from $E_{\text{sing}}^0(v', J)$:

$$E_{\text{sing}}^0(v', J+1) \approx E_{\text{sing}}^0(v', J) + 2(J+1)B_v, \quad (21)$$

$$E_{\text{sing}}^0(v', J-1) \approx E_{\text{sing}}^0(v', J) - 2JB_v. \quad (22)$$

For the analysis of the data presented in Fig. 4, this approximation has a very small effect because it only influences the locations of the two distant singlet levels ($v', J=45$) and ($v', J=44$) that weakly perturb the corresponding triplet components ($v, N=45, J=45$) and ($v, N=45, J=44$). The dominant effect observed in these data is the interaction between the triplet level ($v, N=45, J=46$) and the nearby singlet level ($v', J=46$). The energy splitting of these levels is fully specified by ΔE and the measured values of B_v and A_v for the triplet levels.

Exploratory calculations made it clear that ΔE and $\langle v'|v\rangle$ are significantly correlated. Including them both as fitting parameters does not work well. The reason for the correlation can be easily understood by considering second order perturbation theory. For small A_v , we can approximate the second order shifts in the triplet energies as

$$E_{\text{trip}}(v, N=J, J) - E_{\text{trip}}^0(v, N=J, J) \propto \frac{A_v^2 \langle v'|v\rangle^2}{\Delta E}. \quad (23)$$

In other words, as long as the perturbation is weak, we expect that the effect of $\langle v'|v\rangle$ and ΔE can be represented by a single parameter $\Delta E/\langle v'|v\rangle^2$. We performed several tests to evaluate this approximation. We diagonalized several representative matrices formed by adding Eqs. (17) and (18) and compared the results obtained by invoking second order perturbation theory. For plausible values of the fitting parameters, Eq. (23) is reasonably accurate.

Therefore we implemented our fit by setting $\langle v'|v\rangle=1$, with the understanding that ΔE is an effective parameter that represents the real energy offset divided by a factor that ensures the correct ratio $\Delta E/\langle v'|v\rangle^2$ in Eq. (23). To emphasize this point, we will rename ΔE as Q . The parameter Q may be

also viewed in a more general way. Although we have presented A_v as an adjustable constant, we could also consider an R -dependent function $\mathcal{A}(R)$. In this framework, the fine structure coupling constant of vibrational level v of the $1^3\Delta$ state is

$$A_v = \langle v|\mathcal{A}(R)|v\rangle, \quad (24)$$

and the $^3\Delta-^1\Delta$ mixing is governed by the mixed matrix element

$$\langle v'|\mathcal{A}(R)|v\rangle. \quad (25)$$

The present approach preserves the distinction between $\langle v|\mathcal{A}(R)|v\rangle$ and $\langle v'|\mathcal{A}(R)|v\rangle$ if we interpret Q as a composite parameter that gives a scaled energy offset between the singlet and triplet states:

$$Q = \frac{\langle v|\mathcal{A}(R)|v\rangle^2}{\langle v'|\mathcal{A}(R)|v\rangle^2} \Delta E. \quad (26)$$

For given values of the three fitting parameters A_v , b_F , and Q , we can calculate the energies of the 16 hyperfine levels for a rovibrational level of the $1^3\Delta$ state and a nearby $1^1\Delta$ level. If Q is large, we expect that 12 of these levels will be the unperturbed levels of the $1^3\Delta$ and the other four will be the nearly degenerate states of the $1^1\Delta$ level. As Q gets smaller, we expect an increasing degree of mutual perturbation between the states. We vary the parameters A_v , b_F , and Q to fit only the 12 observed levels that are nominally $1^3\Delta$. Because of our lack of knowledge of the separate values of $\langle v'|v\rangle$ and ΔE in the fitting process, we cannot draw any conclusions about the location of the perturbing $1^1\Delta$ level.

The results of the calculations for the nominally $1^3\Delta$ levels are summarized in Fig. 4. Part (a) of the figure provides an overview of the interaction in the absence of hyperfine structure. The calculated pattern of states is determined by diagonalizing the sum of Eqs. (17) and (18) for $J=44, 45$, and 46 and plotting the appropriate eigenvalues. We have also shifted the energies horizontally to keep the dashed line vertical for all $1^1\Delta-1^3\Delta$ energy differences except near the curve crossing. Part (b) of Fig. 4 shows how our model corresponds very closely to the observed spectra. As v increases from 46 to 49, the appropriate value of Q decreases, corresponding to a closer approach of the unperturbed $J=46$ rovibrational levels. We plot the scans for each value of v in part (b) at a vertical offset that is proportional to the best value of Q ; in this way the experimental scans overlay the theoretical curves. The theoretical curves in part (b), which include hyperfine structure, follow a pattern that is consistent with the simpler behavior shown in part (a), where hyperfine structure is not included. Essentially, the hyperfine interaction splits each level into four states, and there is a complicated pattern of crossings and avoided crossings whenever two sets of four cross. This diagram should make it clear that the anomalous behavior of the 12 nominally $1^3\Delta$ hyperfine levels is caused by the interaction with the rotational levels of a relatively distant $1^1\Delta$ vibrational level.

The fits shown in Fig. (4) for $v=46-48$ were determined by our standard nonlinear least squares program, which is

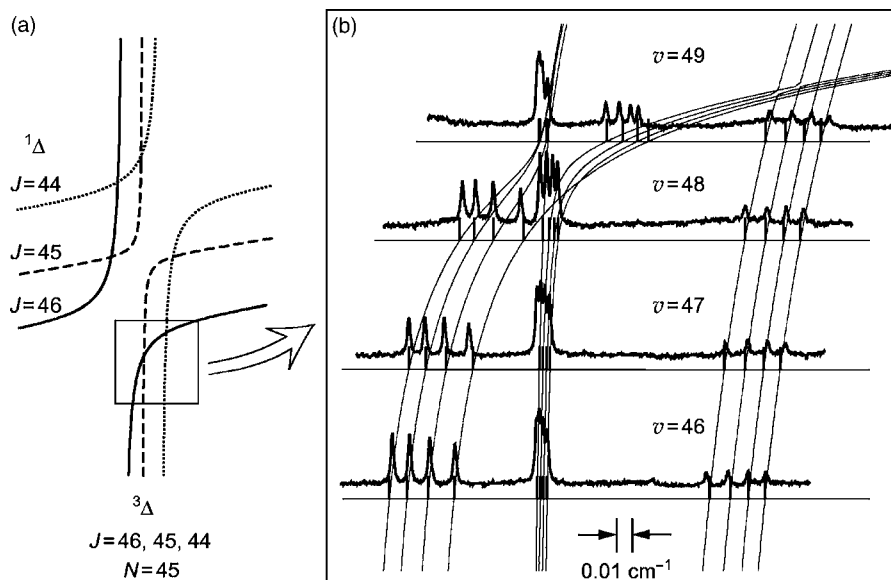


FIG. 4. Comparison of experiment with theory for the ${}^3\Delta-{}^1\Delta$ mixing. The horizontal axis corresponds to measured or calculated energy levels, and the vertical axis is proportional to the ${}^3\Delta-{}^1\Delta$ energy offset. The curves in part (a) illustrate the behavior in the absence of hyperfine structure. Three fine structure levels of a ${}^3\Delta$ state are labeled by $J=46, 45,$ and 44 , and each J level exhibits an interaction with a ${}^1\Delta$ state of the same J . The region shown in the small box in part (a) is enlarged in part (b) and compared with experiment. The experimental scans in (b) have been shifted slightly upward from the horizontal lines. The curves in (a) and (b) do not correspond exactly. The curves in (a) are idealized and are based on constant values of A_v , and $b_F=0$. For the curves in (b), the best-fit values of A_v and b_F determined for each v were fit to polynomials so that the theoretical curves could be smoothly interpolated between the spectra obtained for each v . The calculated curves in (b) corresponding to the hyperfine levels with $J=44$ (that is, the rightmost curves for $v=46-48$) bend to the right because the magnitude of A_v increases as a function of v . The avoided crossing evident in the theoretical curves at the upper right have been exaggerated in order to be visible. The matrix elements between states of the same F but different J are of order 10^{-5} cm^{-1} , much smaller than the hyperfine coupling constant. Accurately drawn crossings would not be resolvable on the present scale.

based on the Levenberg–Marquardt algorithm. We had some difficulty fitting the scans for $v=49$. The problem is that the states shown must be extracted from a larger set of energy levels determined for several values of F , and the identification of the proper states is tricky and must sometimes be done by hand. The fit shown in Fig. (4) for $v=49$ appears to be satisfactory, but it was determined manually by extrapolating $b_F(v)$ and A_v from the values at smaller v , and then trying selected values of Q .

The ${}^1\Delta$ $v=49$ level is the highest level for which we were able to obtain a reliable fit to the fine and hyperfine structure. Levels corresponding to values of v up to 59 were identified. However, the scans for $v \geq 50$ were difficult to interpret; no reasonable set of parameters could be found that would make the calculated spectra resemble the experimental results. It is possible that several ${}^1\Delta$ vibrational levels should be included in our model for each high v of the ${}^1\Delta$ state since the vibrational spacing rapidly decreases as the energy approaches the dissociation limit. In addition, effects due to the ${}^3\Pi$ state might also play a role.

C. Results for A_v and b_F over entire range of v

This section collects and discusses all our data for A_v and $b_F(v)$. Figures 5 and 6 display the results. (The numerical values are tabulated in EPAPS Table II.⁴⁴) Huennekens *et al.*¹ determined the best values of A_v for v in the range $0 \leq v \leq 33$. The analysis was performed for each value of v independently. A linear fit to the vibrational dependence of A_v was determined using all the measured values. The work

described in Sec. IV A determined new values of A_v and $b_F(v)$ for ${}^1\Delta$ levels with $3 \leq v \leq 43$. The data for each v were analyzed separately, and the results for $v=13$ (which is clearly perturbed) were excluded. The work described in Sec. IV B determined A_v and $b_F(v)$ for the ${}^1\Delta$ levels with $44 \leq v \leq 49$, using a theoretical model that included the effect of the nearest ${}^1\Delta$ level. All of these results are shown in Fig. 5. The new results are completely consistent with the older analysis in the region where they overlap, and the values of A_v for larger v join smoothly with the earlier values.

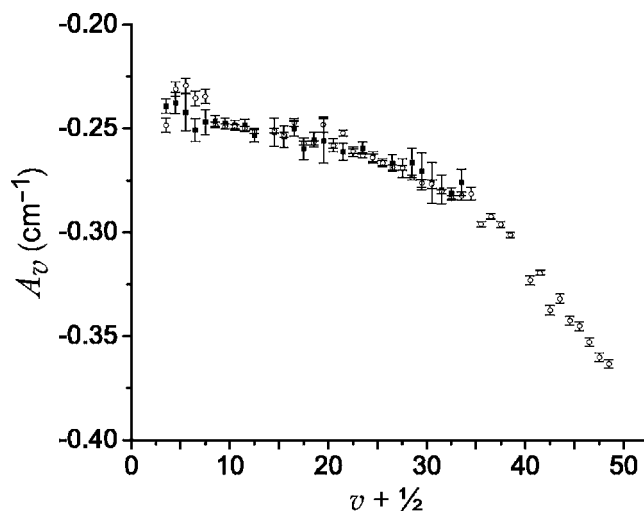


FIG. 5. Fitted values for A_v . The solid squares (■) show the results obtained by Huennekens *et al.*¹ for $3 \leq v \leq 33$, and the open circles (○) show the new values for $3 \leq v \leq 48$ obtained in the present work.

Figure 5 clearly shows the systematic variation in the value of A_v for different values of v . We expect that the dependence on v reflects the dependence of the molecular spin-orbit interaction on the internuclear separation R . For smaller v , A_v depends only weakly on v , presumably because for low vibrational levels, the average value of R is close to that of the $v=0$ state. However, as v increases, the extent of the vibrational motion of the molecule increases, and the average value of A_v has an increasing contribution from large values of R . For large v , the vibrational wave function is strongly peaked at large R , and the limiting value of A_v should be determined by the separated atom limit of $\text{Na}(3s)+\text{K}(3d)$. For a simple estimate of this value, we follow the analysis in Ref. 35, which leads to the relationship $A_v=A/2$ between the molecular spin-orbit constant A_v and the single electron constant A , for the case of a $^3\Delta$ state arising from a $\sigma\delta$ electronic configuration. Hence in the large v limit, we expect A_v to approach one half the potassium $3d$ atomic value, $A_v \rightarrow \frac{1}{2} \times \frac{2}{5} (E_{5/2} - E_{3/2}) \approx \frac{1}{2} \times \frac{2}{5} \times (-2.33 \text{ cm}^{-1})$, or about -0.46 cm^{-1} . The variation in A_v displayed in Fig. 5 is consistent with this asymptotic limit, but more data and analysis are needed for a definitive conclusion. [Note that in Ref. 4 we incorrectly gave the asymptotic limit of A_v for the $3^3\Pi$ state as about -1 cm^{-1} . According to the analysis of Ref. 35, this limiting value should also be -0.46 cm^{-1} .]

Figure 6 shows the values of b_F determined for various values of v . The straight line is a linear least squares fit. The value for small v , 0.011 cm^{-1} , is similar to that found for several other electronic states of NaK.^{1-3,37,48-50} For large v , we expect that b_F should approach a value determined by the separated atom limit, $\text{Na}(3s)+\text{K}(3d)$. In the present case, we attribute the hyperfine interaction entirely to the Na nucleus, and we would expect b_F to be half as large as it is for atomic Na.⁵¹ The argument is that the hyperfine energy U_{hf} for atomic Na can be written $U_{\text{hf}}=b_F^{(\text{atom})}\mathbf{I}\cdot\mathbf{s}$, where \mathbf{s} is the single electron's spin. Near the separated atom limit of NaK, the effect on the energy should be the same, but we write $U_{\text{hf}}=b_F^{(\text{molecule})}\mathbf{I}\cdot\mathbf{S}$. Since \mathbf{S} includes the spins of both of the (indistinguishable) valence electrons of the molecule (one of

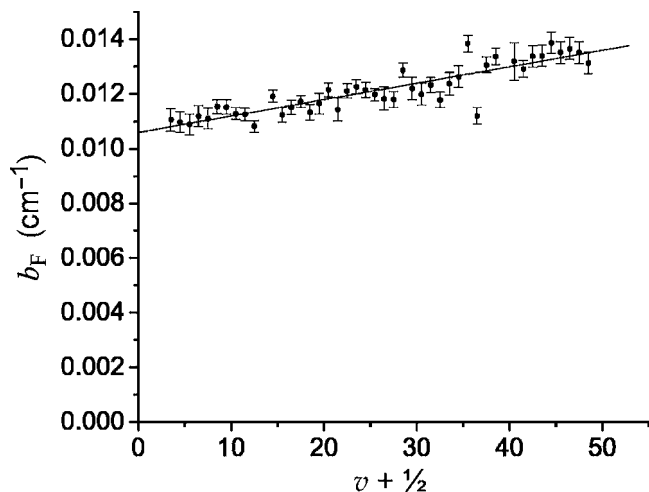


FIG. 6. Fitted values for b_F . Results for the range $3 \leq v \leq 48$ are shown. The behavior of $b_F(v)$ near $v=35$ is not thought to be significant. Nothing was found in the original data to suggest any unusual features.

which is in a Rydberg orbital and, therefore, has little probability of being found at the location of the Na nucleus), the effective Fermi constant must decrease by a factor of two. Hence we expect

$$b_F = 0.5 \times 886 \text{ MHz} = 0.0148 \text{ cm}^{-1}. \quad (27)$$

This limiting value of b_F is consistent with the present measurements.

D. The NaK $1^3\Delta$ potential and long-range behavior

In order to map the NaK $1^3\Delta$ electronic potential, we first fit energies obtained from 622 PFOODR transition frequencies representing 394 $1^3\Delta(v, N, J=N, e/f)$ rovibrational levels (F_2 components) to a standard Dunham expansion^{52,53} using the program DParFit.⁵⁴

$$E(v, N, J=N) = \sum_{i,k} Y_{i,k} \left(v + \frac{1}{2}\right)^i [N(N+1) - \Lambda^2]^k, \quad (28)$$

where $\Lambda=2$ for a Δ state. To first order, the F_2 components are not strongly affected by the spin-orbit and hyperfine interactions, so the Dunham coefficients reported in EPAPS Table III⁴⁴ provide a reasonably accurate representation of the $1^3\Delta(v, N, J=N, e/f)$ level energies. The RMS deviation of the fitted energies from measured values is 0.0079 cm^{-1} .

In the next step, the Dunham coefficients were used to determine a Rydberg-Klein-Rees (RKR) potential for the NaK $1^3\Delta$ state using Le Roy's RKR program.⁵⁵ However, as Beckel and Engelke⁵⁶ pointed out, the Dunham expansion no longer converges for R values that are more than twice the equilibrium separation. In the present case, the highest vibrational levels measured have outer turning points that are more than three times the equilibrium separation. Thus we do not expect that the RKR potential determined here will provide an accurate representation of the long range region of the potential.

We decided to refine the fitted potential using the inverted perturbation approximation (IPA) method.^{57,58} IPA is an iterative approach that attempts to find a potential $V(R)$ such that the calculated rovibrational level energies, $E_{\text{calc}}(v, N, J=N)$, agree with the experimentally measured energies in the least squares sense. We recently described our implementation of this method⁴ using the publicly available IPA code,⁵⁸ slightly modified to make use of subroutines from the program LEVEL⁵⁹ to calculate the rovibrational level energies. Because the IPA method adjusts the potential on a grid of points, it can introduce unphysical wiggles into the results. Even the RKR curve showed some small wiggles high on the inner wall, so we first smoothed the RKR potential by fitting the $v \geq 50$ inner wall turning points to the function

$$R_{\text{min}} = \beta_1 \ln \frac{E - \beta_2}{\beta_3}, \quad (29)$$

which is equivalent to fitting the energies to an exponential $E = \beta_3 \exp(R_{\text{min}}/\beta_1) + \beta_2$. The inner wall turning points were corrected to the fitted values and the outer wall turning points were adjusted to maintain the differences ($R_{\text{max}} - R_{\text{min}}$) calculated in the RKR analysis. The smoothed RKR

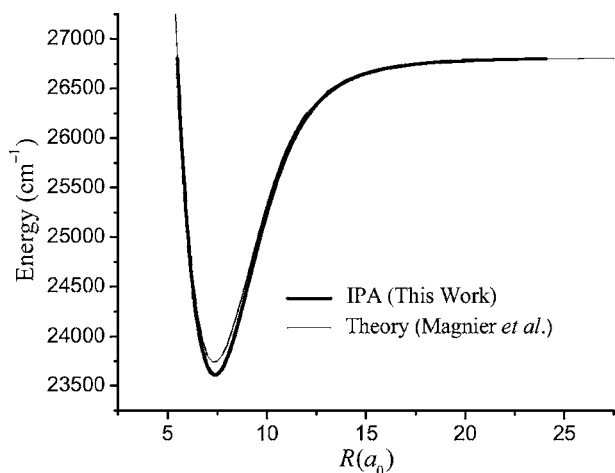


FIG. 7. The IPA potential determined from the present experimental data compared with the theoretical results of Magnier *et al.* (Refs. 46 and 47).

potential (which is reported in EPAPS Table IV⁴⁴) was then used as the initial reference potential in the IPA analysis. The RMS deviation of energies calculated using this smoothed RKR potential from the experimental energies was 0.177 cm^{-1} .

We carried out 13 iterations of the IPA procedure, letting the number of grid points gradually increase from five to 27. After each iteration, the IPA potential was plotted to see if any unphysical wiggles had appeared in the curve. We consider the best fit to be a compromise between reducing the RMS deviation between calculated and experimental level energies on the one hand, and maintaining a smooth curve on the other. The final IPA potential reported here in EPAPS Table V⁴⁴ and plotted in Fig. 7, produced an RMS deviation of 0.026 cm^{-1} between calculated and experimental energies. Figure 7 also shows a comparison of the present IPA $1^3\Delta$ potential with the theoretical results of Magnier *et al.*^{46,47}

Ji *et al.*⁶⁰ have proposed a modification to the Le Roy criterion for the region of validity of the inverse-power expansion in diatomic long-range potentials:

$$R_{\text{LR-m}} = 2\sqrt{3}[\langle nlm|z^2|nlm\rangle_A^{1/2} + \langle n'l'm'|z^2|n'l'm'\rangle_B^{1/2}], \quad (30)$$

where nlm and $n'l'm'$ are the quantum numbers for the valence electrons of atoms A and B, respectively, and the z direction is the internuclear axis. For internuclear separations greater than $R_{\text{LR-m}}$, the potential should approximately follow a simple dependence,

$$V(\infty) - V(R) = \sum_n \frac{C_n}{R^n}, \quad (31)$$

in terms of the long-range dispersion coefficients C_n . For heteronuclear molecules, the C_3 and C_5 resonance terms are zero since no resonant dipole or quadrupole excitations between the different atoms are allowed. Therefore, the R^{-6} van der Waals interaction provides the leading term in this expansion for the NaK $1^3\Delta$ state. Using the formulas of Ji *et al.*,⁶⁰ we calculate $R_{\text{LR-m}} \approx 20.3 a_0$ for the NaK $1^3\Delta$ state, which dissociates to the $\text{Na}(3s_\sigma) + \text{K}(3d_\delta)$ asymptote. Since the present IPA $1^3\Delta$ state potential extends past $24 a_0$, where

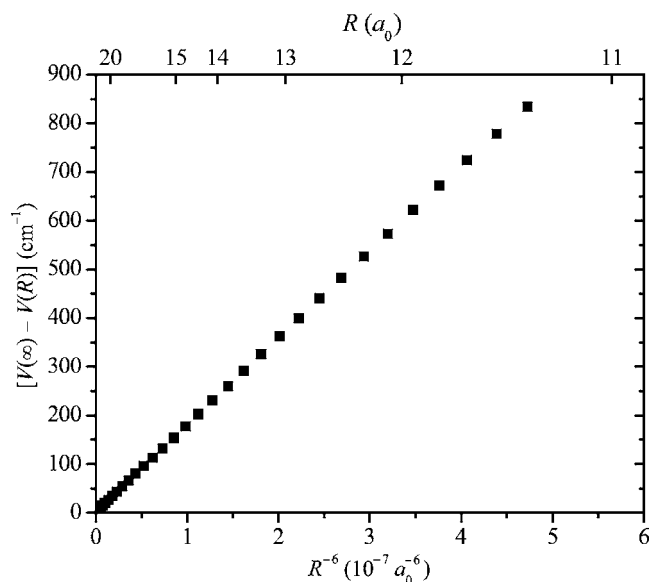


FIG. 8. The binding energy of the $1^3\Delta$ potential is plotted as a function of R^{-6} .

the long-range analysis should be valid, we attempted to determine the leading coefficients, C_6 and C_8 , from these data. We note that the correlation diagram connecting the Hund's case (a) or (b) molecular states near the ground state equilibrium separation and the separated atom dissociation limits shows the NaK $1^3\Delta$ state adiabatically dissociating to the $\text{Na}(3s_{1/2}) + \text{K}(3d_{5/2})$ limit.⁶¹ Thus the $\text{Na}(3s_{1/2}) + \text{K}(3d_{5/2})$ dissociation limit was used in the analysis of the $1^3\Delta$ state in Ref. 1. However, in the present work, the $1^3\Delta$ state has been mapped to large R values that are well past the $3^3\Pi - 1^3\Delta$ curve crossing region. The $1^3\Delta$ potential in this large R region correlates adiabatically to the $\text{Na}(3s_{1/2}) + \text{K}(3d_{3/2})$ dissociation limit, and therefore $V(\infty)$ corresponds to this limit in the present long-range analysis.

Figure 8 shows a plot of $V(\infty) - V(R)$ versus R^{-6} for $R \geq 11.3 a_0$. The dependence is linear over a broad range that extends well inside the modified Le Roy radius. A much more sensitive view of the long-range dependence appears in Fig. 9 which shows a plot of $R^6[V(\infty) - V(R)]$ versus R^{-2} . If C_6 and C_8 are the dominant terms in Eq. (31), it follows that this plot should be a straight line with slope C_8 and intercept C_6 . A linear fit of the data in Fig. 9, corresponding to the long-range region of the IPA potential ($R \geq 11.3 a_0$), yields the values of C_6 and C_8 given in Table II, which include statistical error bars only. However, the dependence of $R^6[V(\infty) - V(R)]$ on R^{-2} shown in Fig. 9 is clearly not linear, and thus the systematic errors in both the intercept and especially the slope are significantly larger than the statistical errors. The C_6 and C_8 coefficients both depend on the range of R values included in the fit. By varying the minimum R value used in the fit, we determined that the C_6 value reported above is accurate to approximately 10%. However, the C_8 coefficient reported above can at best be considered to be an estimate to within a factor of three.

Rérat *et al.*⁶² used the time-dependent gauge-invariant method to calculate the long range C_6 coefficient for the NaK $1^3\Delta$ state. Their result is in good agreement with ours. More

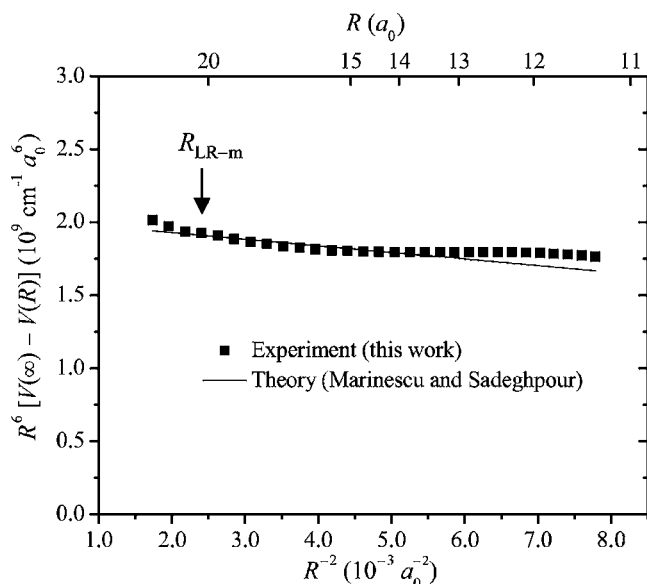


FIG. 9. Reduced plot of the potential. This plot exaggerates the deviation from pure C_6 and C_8 behavior. The agreement with recently calculated values of C_6 and C_8 (Ref. 63) is excellent.

recently Marinescu and Sadeghpour⁶³ calculated C_6 and C_8 values in second order of perturbation theory for all the heteronuclear alkali diatomics. Their results for the NaK $1^3\Delta$ state are also given in Table II. For comparison with the present experimental long-range data, Fig. 9 shows a plot of $C_6 + C_8 R^{-2}$ versus R^{-2} using the C_6 and C_8 values of Marinescu and Sadeghpour.⁶³ The agreement between theory and experiment is excellent. In fact, the theory is probably more accurate than experiment in the present case, since only the last four experimental points on the left in Fig. 9 represent the potential for R values beyond the modified Le Roy radius, and these points correspond to the highest energy levels ($v=56-59$) where the recorded data were limited. The deviation between the experimental and theoretical results at smaller R values (right-hand side of Fig. 9) is probably due to the breakdown of the long-range inverse power series expansion.

V. CONCLUDING REMARKS

We have reported extensive theoretical and experimental studies of rovibrational levels of the $1^3\Delta$ state of NaK for $3 \leq v \leq 59$. We determined a potential curve, and we interpreted the observed patterns of fine and hyperfine structure. Modeling this structure requires using intermediate angular

TABLE II. C_6 and C_8 coefficients. The quoted error estimates for the present experimental results represent only the statistical errors in the least squares fit. Systematic errors are on the order of 10% for C_6 and perhaps a factor of three for C_8 . The theoretical values cited were originally reported in atomic units and have been converted to the units used here.

	$C_6 [10^9 \text{ cm}^{-1} a_0^6]$	$C_8 [10^{10} \text{ cm}^{-1} a_0^8]$
Present work	1.97 ± 0.02	-2.91 ± 0.32
Rérat <i>et al.</i> (Ref. 62)	2.112	
Marinescu and Sadeghpour (Ref. 63)	2.0187	-4.4968

momentum coupling schemes. The interplay between fine and hyperfine coupling terms as the rotational quantum number N changes is analogous to the classic transition between LS and jj coupling as the atomic number changes in the periodic table. For v in the range 44–49, anomalous hyperfine structure could be explained by including perturbations induced by rovibrational levels of the $1^1\Delta$ state. The present work has led to the determination of the coupling constants A_v and b_F over a wide range of v . Further investigation is needed to address the complications that arise for v in the range 50–59.

ACKNOWLEDGMENTS

This work was supported by the National Science Foundation Grant No. PHY-0244767. A.D.W. and J.H.-G. were supported by the NSF REU site grant in the Department of Physics at Lehigh University; A.D.W. was also supported by a Dean's Fellowship from Lehigh University. L.M. was supported by an NSF graduate fellowship. The authors acknowledge helpful conversations with D. L. Huestis and W. C. Stwalley.

- ¹J. Huennekens, I. Prodan, A. Marks, L. Sibbach, E. Galle, T. Morgus, and Li Li, *J. Chem. Phys.* **113**, 7384 (2000).
- ²P. Burns, L. Sibbach-Morgus, A. D. Wilkins, F. Halpern, L. Clarke, R. D. Miles, Li Li, A. P. Hickman, and J. Huennekens, *J. Chem. Phys.* **119**, 4743 (2003).
- ³P. Burns, A. D. Wilkins, A. P. Hickman, and J. Huennekens, *J. Chem. Phys.* **122**, 074306 (2005).
- ⁴L. Morgus, P. Burns, R. D. Miles, A. D. Wilkins, U. Ogba, A. P. Hickman, and J. Huennekens, *J. Chem. Phys.* **122**, 144313 (2005).
- ⁵Li Li and R. W. Field, *J. Phys. Chem.* **87**, 3020 (1983).
- ⁶X. Xie and R. W. Field, *J. Mol. Spectrosc.* **117**, 228 (1986).
- ⁷Li Li and R. W. Field, *J. Mol. Spectrosc.* **123**, 237 (1987).
- ⁸Li Li, Q. Zhu, and R. W. Field, *J. Mol. Spectrosc.* **134**, 50 (1989).
- ⁹Li Li, Q. Zhu, and R. W. Field, *Mol. Phys.* **66**, 685 (1989).
- ¹⁰Li Li, A. M. Lyyra, W. T. Luh, and W. C. Stwalley, *J. Chem. Phys.* **93**, 8452 (1990).
- ¹¹T.-J. Whang, A. M. Lyyra, W. C. Stwalley, and Li Li, *J. Mol. Spectrosc.* **149**, 505 (1991).
- ¹²T.-J. Whang, W. C. Stwalley, Li Li, and A. M. Lyyra, *J. Mol. Spectrosc.* **155**, 184 (1992).
- ¹³Li Li, T. An, T.-J. Whang, A. M. Lyyra, W. C. Stwalley, R. W. Field, and R. A. Bernheim, *J. Chem. Phys.* **96**, 3342 (1992).
- ¹⁴D. S. Chen, L. Li, X. T. Wang, Li Li, Q. Hui, H. Ma, L. Q. Li, X. Y. Xu, and D. Y. Chun, *J. Mol. Spectrosc.* **161**, 7 (1993).
- ¹⁵A. Yiannopoulou, B. Ji, Li Li, M. Li, K. Urbanski, A. M. Lyyra, W. C. Stwalley, and G.-H. Jeung, *J. Chem. Phys.* **101**, 3581 (1994).
- ¹⁶B. Ji, C.-C. Tsai, Li Li, T.-J. Whang, A. M. Lyyra, H. Wang, J. T. Bahns, W. C. Stwalley, and R. J. Le Roy, *J. Chem. Phys.* **103**, 7240 (1995).
- ¹⁷Y. Liu, J. Li, M. Xue, D. Chen, Li Li, and G.-H. Jeung, *J. Chem. Phys.* **103**, 7213 (1995).
- ¹⁸J. T. Kim, H. Wang, C.-C. Tsai, J. T. Bahns, W. C. Stwalley, G. Jong, and A. M. Lyyra, *J. Chem. Phys.* **102**, 6646 (1995), **103**, 9891(E) (1995).
- ¹⁹Li Li, A. Yiannopoulou, K. Urbanski, A. M. Lyyra, B. Ji, W. C. Stwalley, and T. An, *J. Chem. Phys.* **105**, 6192 (1996); **106**, 8626(E) (1997).
- ²⁰J. Li, Y. Liu, H. Gao, M. Xue, D. Chen, and Li Li, *J. Mol. Spectrosc.* **175**, 13 (1996).
- ²¹Y. Liu, J. Li, H. Gao, D. Chen, Li Li, R. W. Field, and A. M. Lyyra, *J. Chem. Phys.* **108**, 2269 (1998).
- ²²J. Li, Y. Liu, H. Chen, H. Gao, J. Xiang, D. Chen, G. Wu, Li Li, and R. W. Field, *J. Chem. Phys.* **108**, 7707 (1998).
- ²³V. S. Ivanov, V. B. Sovkov, Li Li, A. M. Lyyra, G. Lazarov, and J. Huennekens, *J. Mol. Spectrosc.* **194**, 147 (1999).
- ²⁴C. Linton, F. Martin, A. J. Ross, I. Russier, P. Crozet, A. Yiannopoulou, Li Li, and A. M. Lyyra, *J. Mol. Spectrosc.* **196**, 20 (1999).
- ²⁵Li Li and A. M. Lyyra, *Spectrochim. Acta, Part A* **55**, 2147 (1999).
- ²⁶G. Lazarov, A. M. Lyyra, Li Li, and J. Huennekens, *J. Mol. Spectrosc.*

- 196, 259 (1999).
- ²⁷ X. Dai, J. O. Clevenger, Y. Liu, M. Song, J. Shang, D. Chen, R. W. Field, and Li Li, *J. Mol. Spectrosc.* **200**, 120 (2000).
- ²⁸ Li Li, X. Dai, Y. Liu, J. O. Clevenger, R. W. Field, G.-H. Jeung, N. Geum, and A. M. Lyyra, *J. Mol. Spectrosc.* **205**, 139 (2001).
- ²⁹ S. Gerstenkorn and P. Luc, *Atlas du Spectre D'Absorption de la Molécule D'Iode* (Centre National de la Recherche Scientifique, Paris, 1978).
- ³⁰ I. Kovács, *Rotational Structure in the Spectra of Diatomic Molecules* (Elsevier, New York, 1969).
- ³¹ R. N. Zare, A. L. Schmeltekopf, W. J. Harrop, and D. L. Albritton, *J. Mol. Spectrosc.* **46**, 37 (1973).
- ³² J. M. Brown, E. A. Colbourn, J. K. G. Watson, and F. D. Wayne, *J. Mol. Spectrosc.* **74**, 294 (1979).
- ³³ R. N. Zare, *Angular Momentum* (Wiley, New York, 1988).
- ³⁴ D. L. Huestis, in *Atomic, Molecular, and Optical Physics Handbook*, edited by G. W. F. Drake (AIP, New York, 1996).
- ³⁵ H. Lefebvre-Brion and R. W. Field, *The Spectra and Dynamics of Diatomic Molecules* (Elsevier, Amsterdam, 2004).
- ³⁶ C. H. Townes and A. L. Schawlow, *Microwave Spectroscopy* (McGraw-Hill, New York, 1955).
- ³⁷ K. Ishikawa, T. Kumauchi, M. Baba, and H. Katô, *J. Chem. Phys.* **96**, 6423 (1992).
- ³⁸ K. Ishikawa, *J. Chem. Phys.* **98**, 1916 (1993).
- ³⁹ H. Katô, *Bull. Chem. Soc. Jpn.* **66**, 3203 (1993).
- ⁴⁰ W. J. Stevens, D. D. Konowalow, and L. B. Ratcliff, *J. Chem. Phys.* **80**, 1215 (1984).
- ⁴¹ A. Messiah, *Quantum Mechanics* (Wiley, New York, 1966), Vol. II.
- ⁴² R. A. Gottscho, J. B. Koffend, and R. W. Field, *J. Mol. Spectrosc.* **82**, 310 (1980).
- ⁴³ E. U. Condon and G. H. Shortley, *The Theory of Atomic Spectra* (Cambridge University Press, Cambridge, 1991).
- ⁴⁴ See EPAPS Document No. E-JCPSA6-123-007531 for five tables of related information. This document can be reached via a direct link in the online article's HTML reference section or via the EPAPS homepage (<http://www.aip.org/pubservs/epaps.html>).
- ⁴⁵ I. Russier-Antoine, A. J. Ross, M. Aubert-Frécon, F. Martin, and P. Crozet, *J. Phys. B* **33**, 2753 (2000).
- ⁴⁶ S. Magnier and Ph. Millié, *Phys. Rev. A* **54**, 204 (1996).
- ⁴⁷ S. Magnier, M. Aubert-Frécon, and Ph. Millié, *J. Mol. Spectrosc.* **200**, 96 (2000).
- ⁴⁸ P. Kowalczyk, B. Krüger, and F. Engelke, *Chem. Phys. Lett.* **147**, 301 (1988).
- ⁴⁹ P. Kowalczyk, *J. Chem. Phys.* **91**, 2779 (1989).
- ⁵⁰ M. Baba, K. Nishizawa, N. Yoshie, K. Ishikawa, and H. Katô, *J. Chem. Phys.* **96**, 955 (1992).
- ⁵¹ E. Arimondo, M. Inguscio, and P. Violino, *Rev. Mod. Phys.* **49**, 31 (1977).
- ⁵² J. L. Dunham, *Phys. Rev.* **41**, 713 (1932).
- ⁵³ J. L. Dunham, *Phys. Rev.* **41**, 721 (1932).
- ⁵⁴ R. J. Le Roy, DParFit 3.3: A Computer Program for Fitting Diatomic Molecule Spectral Data to Parameterized Level Energy Expressions, Chemical Physics Research Report No. CP-660, University of Waterloo, 2005.
- ⁵⁵ R. J. Le Roy, RKR1 2.0: A Computer Program Implementing the First-Order RKR Method for Determining Diatomic Potential Energy Functions, Chemical Physics Research Report No. CP-657R, University of Waterloo, 2004.
- ⁵⁶ C. L. Beckel and R. Engelke, *J. Chem. Phys.* **49**, 5199 (1968).
- ⁵⁷ A. Pashov, W. Jastrzębski, W. Jaśniecki, V. Bednarska, and P. Kowalczyk, *J. Mol. Spectrosc.* **203**, 264 (2000).
- ⁵⁸ A. Pashov, W. Jastrzębski, and P. Kowalczyk, *Comput. Phys. Commun.* **128**, 622 (2000).
- ⁵⁹ R. J. Le Roy, LEVEL 7.5: A Computer Program for Solving the Radial Schrödinger Equation for Bound and Quasibound Levels, Chemical Physics Research Report No. CP-655, University of Waterloo, 2002.
- ⁶⁰ B. Ji, C.-C. Tsai, and W. C. Stwalley, *Chem. Phys. Lett.* **236**, 242 (1995).
- ⁶¹ Z. J. Jabbour and J. Huennekens, *J. Chem. Phys.* **107**, 1094 (1997).
- ⁶² M. Rérat, M. Mérawa, and B. Honvault-Bussery, *J. Chem. Phys.* **109**, 7246 (1998).
- ⁶³ M. Marinescu and H. R. Sadeghpour, *Phys. Rev. A* **59**, 390 (1999).